Optics Letters

High-stability, linearly polarized mode-locking generation from a polarization-maintaining fiber oscillator around 2.8 μm

HONGYU LUO, YONGZHI WANG, JIANFENG LI,* AND YONG LIU

State Key Laboratory of Electronic Thin Films and Integrated Devices, School of Optoelectronic Science and Engineering, University of Electronic Science and Technology of China (UESTC), Chengdu 610054, China
**Corresponding author: lijianfeng@uestc.edu.cn*

Received 22 June 2021; revised 11 August 2021; accepted 19 August 2021; posted 23 August 2021 (Doc. ID 434999); published 9 September 2021

In this Letter, a high-stability, linearly polarized mode-locked polarization-maintaining (PM) Er^{3+}-doped fluoride fiber oscillator at ~2.8 μm is presented for the first time, to the best of our knowledge, where an InAs-based semiconductor saturable absorber mirror is used as the mode locker, and a film polarizer is employed for maintaining the linearly polarized oscillation. In the free-running state, stable linearly polarized mode-locked pulses ($\tau = 44$ ps and $P = 446$ mW) at 2.795 μm, with a high polarization extinction ratio of >23 dB and a low integrated relative intensity noise of 0.087% [1 Hz–10 MHz], have been achieved, which can be strongly immune to external mechanical perturbations. By introducing a ruled reflective diffraction grating into the cavity in a Littman configuration, the continuous wavelength tuning of the linearly polarized mode-locked pulses in the range of 2717–2827 nm is obtained as well. To the best of our knowledge, this marks the first demonstration of a linearly polarized PM fiber oscillator in the >2.5 μm mid-infrared region.

https://doi.org/10.1364/OL.434999

The mid-infrared ultrashort pulsed laser source has become a potential tool to provide excellent service for many fields, e.g., laser surgery [1], polymer processing [2], strong-field physics [3], high-harmonic generation [4], and ultrafast imaging [5]. At the wavelengths near 3 μm, targeting the strong absorption bands of hydroxyapatite and water, the laser has exhibited the remarkable merits in minimally invasive surgery [1]. In the most recent decade, the mode-locked fiber oscillator has been developed into one of the promising platforms for mid-infrared ultrashort pulses generation.

Until now, three typical rare-earth ions including Er^{3+}, Ho^{3+}, and Dy^{3+} have been doped into low-phonon-energy fluoride host fibers to show efficient lasing at ~3 μm [6–8]. Based on these platforms, various mechanisms such as material saturable absorption [9,10], frequency shift feedback [11–13], and nonlinear polarization rotation (NPR) [14–17] have been used for mode locking. In comparison to the latter two, which even enable the linearly polarized outputs due to the used polarization-dependent devices, the mode-locking scheme induced by material saturable absorbers (SAs) owns the superior structure because no additional devices are needed. Recently, an all-fiber version of a 2.8 μm mode-locked Er^{3+}-doped fluoride fiber oscillator using a black phosphorus (BP) SA has been also demonstrated by Qin *et al.* [18].

As the pioneer of SAs, the prototype of semiconductor SA mirror (SESAM) was applied in mode locking a 860 nm Ti:sapphire laser as early as 1990 [19]. Until 2012, however, the first, to the best of our knowledge, commercial SESAM available for the mid-infrared was developed and started to serve the ~3 μm mode-locked fiber oscillator [9]. In the following decade, its excellent reliability and stability and the ability of customizing the parameters always kept it favorable [10,20–22] despite the limited operation wavelength of close to 3.5 μm [23], although many contemporaneously emerged nonlinear nanomaterials, e.g., graphene, BP, WSe_2, gold nanowires [18,24–27], were also employed as mid-infrared mode lockers. Using a SESAM, the maximum average power of the ~3 μm picosecond (ps)-scale mode-locked pulses from a fiber oscillator has reached the recorded 1.05 W [10]. With a suitable diffraction grating, the wavelength tuning of the mode-locked Er^{3+}- and Ho^{3+}-doped fluoride fiber oscillators in the range of 2.7–2.9 μm have been also reported [21,22].

It is well known that the environmental stability for a laser must be considered before its employment in practical applications. All of the reported mid-infrared mode-locked fiber oscillators, however, were based on non-polarization-maintaining (PM) fiber cavities. Therefore, they suffered from serious enviromental instability due to sensitivity to mechanical perturbations and significant temperature variations as a result of the induced change of fiber birefringence. The use of the PM fiber is the most effective method to eliminate the instability. In addition, the randomly polarized outputs from most previous material SAs mode-locked non-PM fiber systems are not yet suitable for some polarization-sensitive applications, e.g., parametric conversion, frequency doubling, harmonic generation, coherent combining.

In this Letter, we adopted a PM Er^{3+}-doped fluoride fiber as the gain medium and a SESAM as the mode locker to present

the high-stability, linearly polarized ps-scale pulse outputs from a ~2.8 μm oscillator. It can yield a maximum average power of 446 mW with a high polarization extinction ratio (PER) of >23 dB and a low integrated relative intensity noise (RIN) of 0.087% [1 Hz-10 MHz], while the wavelength can be also tuned in the range of 2717–2827 nm. To the best of our knowledge, this is the first demonstration of a linearly polarized PM fiber oscillator at >2.5 μm.

In our oscillator, the newly developed PM double-clad 7 mol.% Er^{3+}-doped fluoride fiber (Le Verre Fluoré, France) is the most key component since it causes the high-stability and linearly polarized operation. The inset of Fig. 1 shows its zoomed cross section. It has a core diameter of 15 μm (NA = 0.12) and an inner clad diameter of 260 μm (NA = 0.4), where its circular symmetry is broken by two parallel flats separated by 240 μm, and the core/clad eccentricity is about 8 μm. Its linearly polarized light propagation is mainly originated from the two air-gaps. For a PM fiber, the beat length is an indispensable parameter and was characterized by us based on the conoscopic interference phenomenon [28]. Figure 1(a) shows the used configuration, in which a halogen lamp acts as the source, and a segment of a 64 cm PM fiber is used for the test. A polarizer and an analyzer are located on two sides of the PM fiber, respectively, for getting the conoscopic interference. A monochromator involving an InSb detector is used to capture the signal. First, the polarizer and analyzer were oriented to get the minimum signal, where their angles were both recorded as 0°. Note that their polarization axes cannot be parallel to the fast or slow axis of the PM fiber in order to observe the conoscopic interference phenomenon. In this case, the signal is labeled "Signal 1". Then, the analyzer was oriented at 90°, and the corresponding signal is labeled "Signal 2". Thus, the beat length can be calculated as the following expression:

$$L_B = \frac{\Delta\lambda}{\lambda} \cdot L, \tag{1}$$

where L_B is the beat length, $\Delta\lambda$ is the period, λ is the wavelength, and L is the fiber length. To get better accuracy on the beat length measurement, Signal 1/Signal 2 was also calculated as plotted in Fig. 1(b). At 2.79 μm, $\Delta\lambda = 0.18$ μm, as a result,

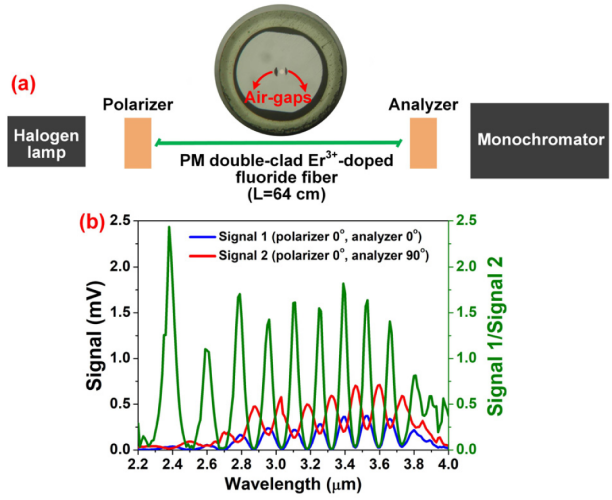

Fig. 1. (a) Configuration of the beat length measurement setup; inset: the zoomed cross section of the PM fiber. (b) Signals as a function of the wavelength.

L_B is calculated to be 4.13 cm when $L = 64$ cm. In addition, the fast- and slow-axis propagation losses have also been measured based on an in-house continuous wave (CW) fiber laser at ~2.8 μm. The fitted fast- and slow-axis propagation losses of 42.5 and 43.8 dB/km, respectively, are quite close to 40 dB/km given by the manufacturer, measured using a broadband source.

The configuration of the linearly polarized mode-locked PM Er^{3+}-doped fluoride fiber oscillator is shown in Fig. 2. The pump source is a high-power 976 nm laser diode (LD), which can output a maximum power of 100 W from its multimode pigtail with a core diameter of 105 μm (NA = 0.22). The fiber length is 4 m, which can provide enough gain. The fiber end close to the LD was perpendicularly cleaved as the output coupler with the aid of 4% Fresnel reflection, and the pump laser is launched into the inner clad using two lenses (L1 and L2) with a 77% efficiency. Between the two lenses, a dichroic mirror (DM), placed at an angle of 45°, is used to guide the laser for measurements after purifying using a bandpass filter (BF). While the other end of the fiber was angle-cleaved at 8° to avoid the parasitic lasing. In the free-running alignment, the laser from the angle-cleaved fiber end is collimated and focused, using another two lenses (L3 and L4) with a 1:2 demagnification, onto a commercial SESAM (BATOP, SAM-3000-33-10ps-x), which has a modulation depth of 18%, a non-saturable loss of 15%, and a saturation fluence of 70 $\mu J/cm^2$ at 3.0 μm. To maintain the linearly polarized oscillation at ~2.8 μm, an infrared film polarizer (FP) with a nominal extinction ratio of >60 dB and a transmission of 83% in this band is introduced into the cavity, before which another of same DM is used to remove the residual pump, thus avoiding the heat damage of the FP. In the wavelength-tunable alignment, the DM is replaced by a ruled reflection diffraction grating (RRDG, Thorlabs, 450 grooves/mm, blaze wavelength = 3.1 μm, blaze angle = 32°) in a Littman configuration, of which the first-order diffraction is resonated by the SESAM, and the zeroth-order diffraction is released out of the cavity. The power is recorded using a thermal power sensor (Thorlabs, S405C). The temporal signal is captured using a 250 MHz bandwidth (HgCd)Te photodetector

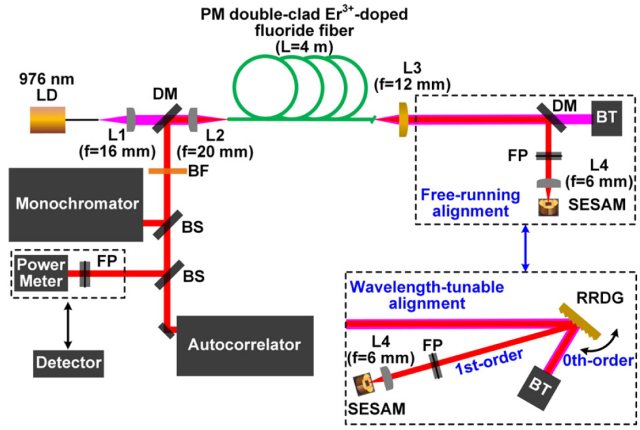

Fig. 2. Configuration of the linearly polarized mode-locked PM Er^{3+}-doped fluoride fiber oscillator with the free-running and wavelength-tunable alignments. LD, laser diode; L1, B270 optical crown glass aspheric lens; L2, CaF_2 plano-convex spherical lens; L3, ZnSe aspheric lens; L4, black diamond aspheric lens; DM, dichroic mirror (45°, T > 95% at 976 nm and R > 95% at ~2.8 μm); BT, beam trap; FP, film polarizer; RRDG, ruled reflective diffraction grating; BF, bandpass filter (2.5–3 μm); BS, beam splitter (T:R = 8:2).

(VIGO, PCI-2TE-12) connecting with a 500 MHz digital oscilloscope. The radio frequency (RF) signal is recorded by an 18 GHz electrical spectrum analyzer (ESA), while the optical spectrum is recorded by a monochromator with a ∼0.4 nm resolution at ∼3 μm (Princeton Instruments Acton SP2300). The temporal width of mode locking is characterized via a commercial autocorrelator (APE, PulseCheck MIR).

First, the FM was rotated to keep its polarization axis parallel to the PM fiber fast axis, since we identified that the linearly polarized oscillation along the fast axis had a higher output power and PER.

In the free-running alignment, stable CW mode locking (CWML) was easily achieved when the pump power was increased beyond 0.73 W, without any Q-switched mode-locking signs. This state could be maintained until the pump power reached 2.7 W, at which the temporal pulse trains were captured, as shown in Fig. 3(a). The pulse-to-pulse interval of 45.4 ns, matching well with the cavity round trip time (fiber length = 4 m, free-space length = 0.8 m) implies the fundamental mode-locking operation. Figure 3(b) and its inset show the RF spectra within 2 and 800 MHz scan ranges, respectively. The up to ∼70 dB signal-to-noise ratio (SNR) of the fundamental beat note at 22.03 MHz is located at the typical level of stable mode locking, and the smooth roll-off of the higher harmonics peaks with no modulations, due mainly to the limited bandwidth of the detector, indicates that no multiple pulses existed. The corresponding optical spectrum is plotted in Fig. 3(c), showing a center wavelength of 2794.6 nm and a 3 dB bandwidth of 2.2 nm. Figure 3(d) gives the measured autocorrelation (AC) trace. Assuming a Gauss profile, the deduced pulse width of 44 ps yields a large time bandwidth product (TBP) of 3.7 [10,25,26], indicating a large chirp involved, mainly caused by the large intra-cavity dispersion (−0.376 ps^2 [14]). If further increasing the pump power, the CW operation would terminate the CWML due to the over-saturation of the SESAM instead of damage, since the CWML could be achieved again once recovering the pump power. Note that the position of the SESAM was always kept unchanged in the process.

Operating in the stable mode-locking state, the evolutions of the average power and PER with the pump power were recorded,

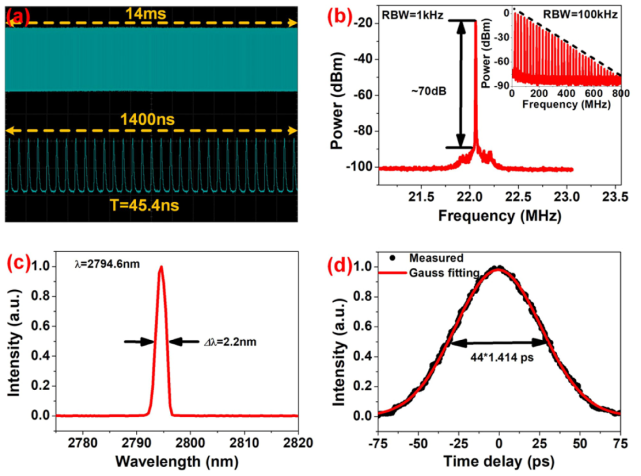

Fig. 3. Free-running mode-locking characteristics in the time and spectrum domains. (a) Temporal behaviors. (See Visualization 1.) (b) RF spectra within the scan ranges of 2 and 800 MHz (inset). (c) Optical spectrum. (d) Autocorrelation (AC) trace with a Gauss fitting.

as shown in Fig. 4(a). It is seen that the average power varies with the pump power with a great linearity. At the pump power of 2.7 W, the maximum average power of 446 mW with a slope efficiency of 18% is obtained, while there is only a slight fluctuation between 23.06 and 24.03 dB for PER, suggesting the great linearly polarized feature of the oscillator. Figure 4(b) plots the corresponding power and PER variations with the time. The low normalized root mean square (RMS) deviations of 0.53% and 0.21% for the power and PER, respectively, indicate that the laser is quite stable. Moreover, the environmental stability of the oscillator was intuitively checked as well. By vibrating the fiber, the PM oscillator exhibited a strong immunity, in contrast to another non-PM mode-locked Er^{3+}-doped fluoride fiber oscillator built by us, in which the same SESAM and a segment of 3.1 m non-PM fiber with identical parameters [15] were used (see Visualization 1).

In addition, it is important to evaluate the noise characteristics of the oscillator. Figure 5 shows the single sideband (SSB) RIN trace of the first harmonic and the corresponding integrated RMS RIN of the PM cavity as well as that of the non-PM cavity mentioned above. The availability of the signal noise can be identified by the lower noise floor of the instruments, including ESA and photodetector. It is seen that the PM cavity has a lower SSB RIN in almost the whole frequency range of 1 Hz–10 MHz. Integrating over this range, the RIN is calculated to be 0.087%, lower than that (i.e., 0.406%) of the non-PM cavity. Over a smaller integrated range of 10 Hz–10 MHz, the RIN even drops to 0.021% by a factor of four. These results imply that the PM system can suppress the noise better.

In the wavelength-tunable alignment, the output characteristics of the mode-locked pulses as the varied wavelength were studied. By rotating the RRDG, the optical spectrum and average power at the pump power of 2.7 W were simultaneously recorded, as shown in Figs. 6(a) and 6(b), respectively. It is seen that the wavelength can be continuously tuned within

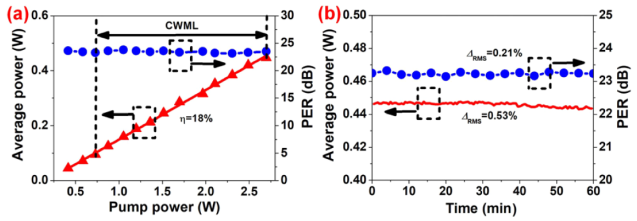

Fig. 4. Free-running mode-locking output average power and PER as a function of the (a) pump power and (b) time within 1 h.

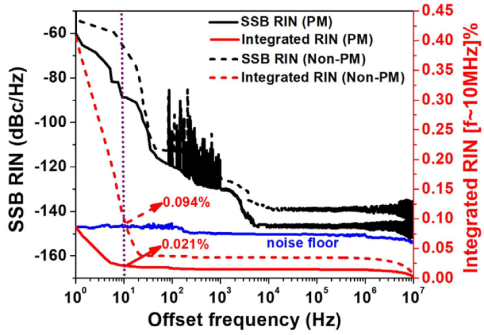

Fig. 5. Single sideband (SSB) RIN traces and integrated RMS RINs of the mode-locked PM and non-PM Er^{3+}-doped fluoride fiber oscillators and the noise floor of the instruments.

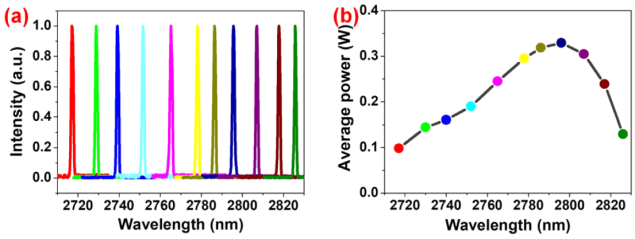

Fig. 6. Wavelength-tunable mode-locking characteristics. (a) Optical spectra and (b) output average power when tuning the wavelength.

the ~110 nm range of 2716.8–2826.6 nm, comparable to that of a non-PM counterpart [22], while the 3 dB bandwidth is narrowed to ~1.3 nm owing to the effect of the grating. With tuning towards the long wavelength, the average power increases first and reaches the maximum at the wavelength of 2796.2 nm, close to the free-running wavelength, and then decreases, corresponding to the intra-cavity gain profile. Although the evolution of the larger pulse width with the tuned wavelength was not characterized, limited by the maximum scan range of 150 ps of the used autocorrelator, it should have a similar behavior to the previously reported non-PM counterpart [22], due to the almost unchanged 3 dB bandwidth, where only a slight fluctuation of the pulse width was observed.

In summary, we demonstrate a high-stability, linearly polarized mode-locked PM Er^{3+}-doped fluoride fiber oscillator in the 2.8 μm band based on an InAs-based SESAM, for the first time, to the best of our knowledge. In the free-running state, stable mode-locked pulses at 2794.6 nm, immune to external mechanical perturbations, have been achieved, giving a maximum average power of 446 mW, a pulse width of 44 ps, a PER of >23 dB, and an integrated RIN of 0.087% [1 Hz–10 MHz]. By introducing a RRDG in a Littman configuration into the cavity, the wavelength of the linearly polarized mode-locked pulses is able to be continuously tuned in the range of 2717–2826 nm. To the best of our knowledge, this is even the first linearly polarized PM fiber oscillator in the >2.5 μm mid-infrared region. In the future, the PM Er^{3+}-doped fluoride fiber can be used in a NPR cavity with a careful walk-off compensation for high-stability femtosecond pulse generation and in a dual-wavelength pumped cavity for linearly polarized laser generation at the longer wavelength of ~3.5 μm.

Funding. National Natural Science Foundation of China (62005040, U20A20210, 61421002); Fundamental Research Funds for the Central Universities (ZYGX2020KYQD003, ZYGX2019Z012); Sichuan Province Science and Technology Support Program (2021YJ0368).

Acknowledgement. The authors thank Thibaud Berthelot (Le Verre Fluoré, France) for providing the PM fiber beat length measurement data.

Disclosures. The authors declare no conflicts of interest.

Data Availability. Data underlying the results presented in this paper are not publicly available at this time but may be obtained from the authors upon reasonable request.

REFERENCES

1. S. Amini-Nik, D. Kraemer, M. L. Cowan, K. Gunaratne, P. Nadesan, B. A. Alman, and R. J. D. Miller, PLoS One **5**, e13053 (2010).
2. J.-P. Berube, C. Frayssinous, J. Lapointe, S. Duval, V. Fortin, and R. Vallée, Opt. Express **27**, 31013 (2019).
3. B. Wolter, C. Lemell, M. Baudisch, M. G. Pullen, X. M. Tong, M. Hemmer, A. Senftleben, C. D. Schröter, J. Ullrich, R. Moshammer, J. Biegert, and J. Burgdörfer, Phys. Rev. A **90**, 063424 (2014).
4. T. Popmintchev, M.-C. Chen, D. Popmintchev, P. Arpin, S. Brown, S. Ališauskas, G. Andriukaitis, T. Balčiunas, O. D. Mücke, A. Pugzlys, A. Baltuška, B. Shim, S. E. Schrauth, A. Gaeta, C. Hernandez-Garcia, L. Plaja, A. Becker, A. Jaron-Becker, M. M. Murnane, and H. C. Kapteyn, Science **336**, 1287 (2012).
5. C. I. Blaga, J. Xu, A. D. DiChiara, E. Sistrunk, K. Zhang, P. Agostini, T. A. Miller, L. F. DiMauro, and C. D. Lin, Nature **483**, 194 (2012).
6. Y. O. Aydin, V. Fortin, R. Vallée, and M. Bernier, Opt. Lett. **43**, 4542 (2018).
7. S. Crawford, D. D. Hudson, and S. D. Jackson, IEEE Photon. J. **7**, 1502309 (2015).
8. V. Fortin, F. Jobin, M. Larose, M. Bernier, and R. Vallée, Opt. Lett. **44**, 491 (2019).
9. J. Li, D. D. Hudson, Y. Liu, and S. D. Jackson, Opt. Lett. **37**, 3747 (2012).
10. P. Tang, Z. Qin, J. Liu, C. Zhao, G. Xie, S. Wen, and L. Qian, Opt. Lett. **40**, 4855 (2015).
11. M. R. Majewski, M. Pawliszewska, and S. D. Jackson, Opt. Express **29**, 19159 (2021).
12. M. Pawliszewska, M. R. Majewski, and S. D. Jackson, Opt. Lett. **45**, 5808 (2020).
13. R. I. Woodward, M. R. Majewski, and S. D. Jackson, APL Photon. **3**, 116106 (2018).
14. S. Duval, M. Bernier, V. Fortin, J. Genest, M. Piché, and R. Vallée, Optica **2**, 623 (2015).
15. H. Luo, J. Yang, J. Li, and Y. Liu, Opt. Lett. **46**, 841 (2021).
16. S. Antipov, D. D. Hudson, A. Fuerbach, and S. D. Jackson, Optica **3**, 1373 (2016).
17. Y. Wang, F. Jobin, S. Duval, V. Fortin, P. Laporta, M. Bernier, G. Galzerano, and R. Vallée, Opt. Lett. **44**, 395 (2019).
18. Z. Qin, G. Xie, J. Ma, P. Yuan, and L. Qian, Photon. Res. **6**, 1074 (2018).
19. U. Keller, W. H. Knox, and H. Roskos, Opt. Lett. **15**, 1377 (1990).
20. A. Haboucha, V. Fortin, M. Bernier, J. Genest, Y. Messaddeq, and R. Vallée, Opt. Lett. **39**, 3294 (2014).
21. C. Wei, H. Shi, H. Luo, H. Zhang, Y. Lyu, and Y. Liu, Opt. Express **25**, 19170 (2017).
22. Y. Shen, Y. Wang, H. Chen, K. Luan, M. Tao, and J. Si, Sci. Rep. **7**, 14913 (2017).
23. Z. Fang, C. Zhang, J. Liu, Y. Chen, and D. Fan, Opt. Laser Technol. **141**, 107131 (2021).
24. G. Zhu, X. Zhu, F. Wang, S. Xu, Y. Li, X. Guo, K. Balakrishnan, R. Norwood, and N. Peyghambarian, IEEE Photon. Technol. Lett. **28**, 7 (2016).
25. Z. Qin, G. Xie, C. Zhao, S. Wen, P. Yuan, and L. Qian, Opt. Lett. **41**, 56 (2016).
26. C. Guo, J. Wei, P. Yan, R. Luo, S. Ruan, J. Wang, B. Guo, P. Hua, and Q. Lue, Appl. Phys. Express **13**, 012013 (2020).
27. H. Luo, S. Li, X. Wu, Z. Kang, J. Li, G. Qin, W. Qin, and Y. Liu, Opt. Lett. **46**, 1562 (2021).
28. J. Mi, C. Zhang, Z. Li, and Z. Wu, J. Optoelectron. Laser **17**, 1704 (2006).